
MACHINE LEARNING BASED LENS-FREE SHADOW IMAGING TECHNIQUE FOR FIELD-PORTABLE CYTOMETRY *

Rajkumar Vaghshiya^{1,4}, Sanghoon Shin^{2,4}, Varun Chauhan¹, Kaushal Kapadiya¹, Smit Sanghavi¹, Sungkyu Seo^{2,5},
and Mohendra Roy^{3,5}

¹*Department of Computer Engineering, Pandit Deendayal Energy University, Gandhinagar, India*

²*Department of Electronics and Information Engineering, Korea University, Sejong 30019, Korea*

³*Department of Information and Communication Technology, Pandit Deendayal Energy University, Gandhinagar 38207, India*

⁴*These authors contributed equally to this study*

⁵*Corresponding authors*

ABSTRACT

Lens-free Shadow Imaging Technique (LSIT) is a well-established technique for the characterization of microparticles and biological cells. Due to its simplicity and cost-effectiveness, various low-cost solutions have been evolved, such as automatic analysis of complete blood count (CBC), cell viability, 2D cell morphology, 3D cell tomography, etc. The developed auto characterization algorithm so far for this custom-developed LSIT cytometer was based on the hand-crafted features of the cell diffraction patterns from the LSIT cytometer, that were determined from our empirical findings on thousands of samples of individual cell types, which limit the system in terms of induction of a new cell type for auto classification or characterization. Further, its performance is suffering from poor image (cell diffraction pattern) signatures due to its small signal or background noise. In this work, we address these issues by leveraging the artificial intelligence-powered auto signal enhancing scheme such as denoising autoencoder and adaptive cell characterization technique based on the transfer of learning in deep neural networks. The performance of our proposed method shows an increase in accuracy >98% along with the signal enhancement of >5 dB for most of the cell types, such as Red Blood Cell (RBC) and White Blood Cell (WBC). Furthermore, the model is adaptive to learn new type of samples within a few learning iterations and able to successfully classify the newly introduced sample along with the existing other sample types.

Keywords Artificial Intelligence · Lens-Free Shadow Imaging Technique · Cell-line Analysis · Cell Signal Enhancement · Deep Learning

1 Introduction

Lens-free Shadow Imaging Technique (LSIT) is a well-established technique for the characterization of microparticles and biological cells [1]. This technique is widely popular for its simple imaging structure and cost-effectiveness. It comprises a lens-less detector such as a complementary metal-oxide semiconductor (CMOS) image sensor, a semi-coherent light source, such as light-emitting diode (LED), and a disposable cell chip (C-Chip). The absence of lens or other optical arrangements allows it to fit into a very small space, thereby reducing the size of the overall system as described in Figure 1a, the LSIT platform (Cellytics) built within a dimension of $100 \times 120 \times 80$ mm³. Since this arrangement consists of a few components, most of which are easily available and at a low price, therefore it reduces the overall cost of the system [2]. This simple and cost-effective nature facilitates the feasibility of the LSIT for applications in the field of point-of-care systems or telemedicine systems [3, 4, 5].

* *Citation:* Vaghshiya, R.; Shin, S.; Chauhan, V.; Kapadiya, K.; Sanghavi, S.; Seo, S.; Roy, M. Machine Learning Based Lens-Free Shadow Imaging Technique for Field-Portable Cytometry. *Biosensors* 2022, 12, 144. <https://doi.org/10.3390/bios12030144>

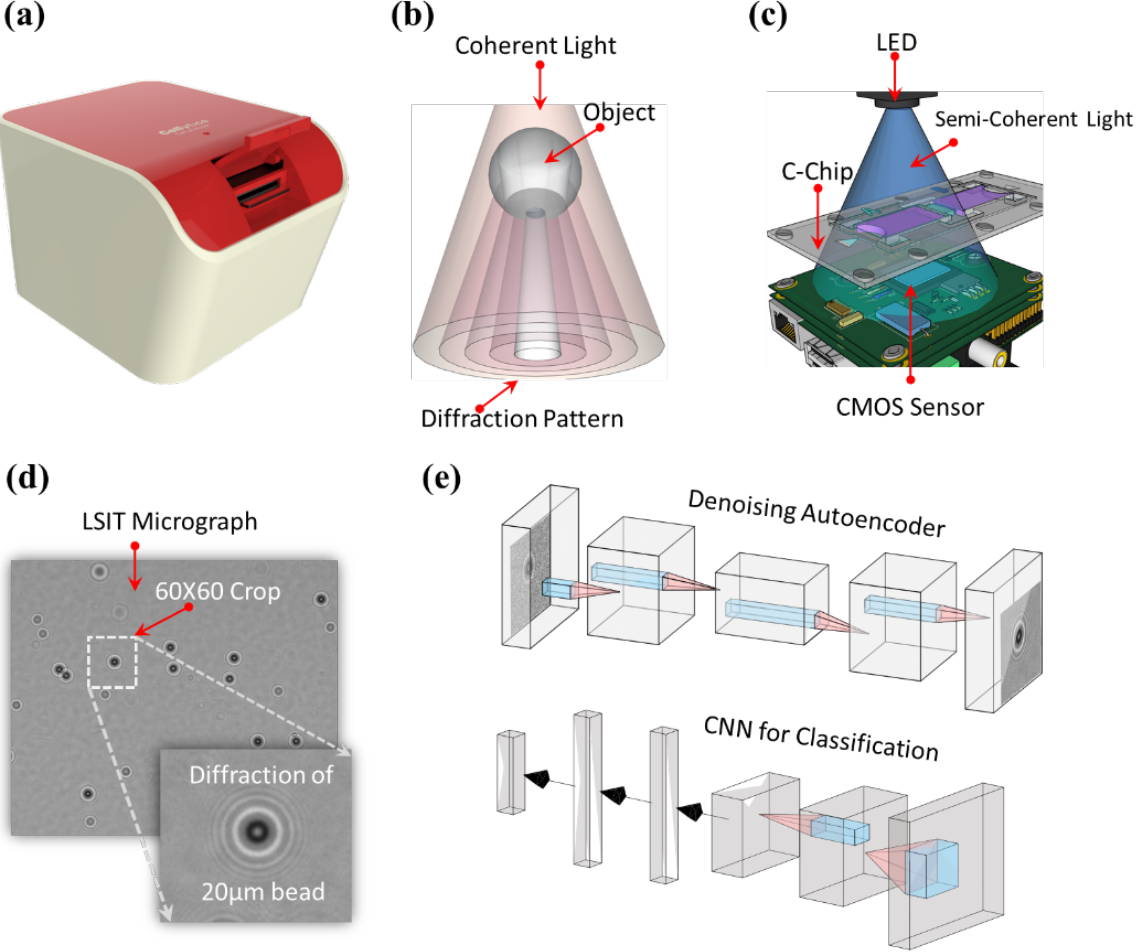


Figure 1: Schematics of the LIST setup and the proposed neural network architecture for the auto characterization of LSIT micrographs. (a) LSIT platform (Celllytics) (b) schematic of the principle of diffraction, i.e., shadow, pattern generation of a micro-object, (c) schematic of the LSIT imaging setup showing the simplicity of the setup, (d) schematic of the dataset creation process by automatic cropping individual cell diffraction pattern from the whole LSIT micrograph, (e) the schematic of the proposed denoising and classification architecture. Here, the denoising autoencoder enhances the signal of the individual cells which is then fed to the CNN module for classification.

Recent advancements in machine learning, especially deep learning, have facilitated many applications concerning medical diagnostics [6, 7, 8, 9, 10, 11, 12], and have been widely adopted in the field of microscopy [13, 14, 15]. Especially, deep learning has been incorporated with the LSIT [14], where it has been used to enhance the resolution of the LSIT micrographs [16] and enabled polarization-based holographic microscopy [17].

In our previous work, we have successfully developed the LSIT imaging system for the complete blood count using an analytical model based on handcrafted features [3] that can automatically segment out the individual cells from a whole frame LSIT micrograph and subsequently analyze them based on the handcrafted parameters. However, the performance of the system is dependent on the uniform illumination as well as the strong signatures of the microparticle samples. Since the diffraction signature of a microparticle depends on the size as well as the signal-to-noise ratio of the particle, therefore any background noise can affect the overall performance of the auto characterization system. Further, the handcrafted approach of finding the features for every additional cell line is time-consuming and prone to subjective errors. To address these limitations, in this work, we have developed an artificial intelligence (AI) powered signal enhancement scheme for the LSIT micrographs that can enhance the signal quality (signal to noise ratio (SNR)) for various cell lines in a heterogeneous cell sample. For this, we employed the autoencoder-based denoising scheme [18]. Further, we have developed an auto characterization method based on a convolutional neural network [19, 20] (CNN) architecture to classify the various cell lines from the LSIT micrograph. Here, we have first introduced the transfer of

learning scheme in a neural network, which can leverage the feasibility to introduce new cell types to the algorithm and thus learn their characteristics within a few iterations. Thus, the LSIT platform saves time and computation resources required to learn to classify the additional cell types along with the existing ones.

In this article, we have described the detailed methods adopted for the designing as well as optimization of various parameters to design a suitable model with better accuracy. These optimized models are simple and light-weight, and require a smaller number of samples for effectively learning the cell signatures. The details are as given in the following sections.

2 Methods

2.1 LSIT Imaging Setup

The schematic of our proposed setup (Figure 1a) is as shown in Fig. 1. When light from the coherent or semi-coherent source passes through a micro-object, it produces characteristic diffraction, i.e., a shadow, pattern of the object [21, 22] as shown in Fig. 1b. These diffraction patterns are prominent just beneath the sample, typically a few hundred micrometers away from the sample plane, from where they are captured using a high-density image sensor such as CCD or CMOS [21] (Fig. 1c). As these signatures are significant enough to be captured by the bared image sensor, it does not require any kind of lens arrangement [23]. In our proposed setup, we used a pinhole conjugated semi-coherent LED light source with a peak wavelength of 470 ± 5 nm (HT-P318FCHU-ZZZZ, Harvatek, Hsinchu, Taiwan). The diffraction patterns were captured using a 5-megapixel CMOS image sensor (EO-5012M, Edmund Optics, Barrington, NJ, USA), and a custom-developed C-Chip (Infino, Seoul, Korea) was used to hold the cell samples [2, 4, 5]. All these components can fit in a compact dimension of $100 \text{ mm} \times 120 \text{ mm} \times 80 \text{ mm}$. Due to the absence of a lens-based setup, the field-of-view of this system is about 20 times that of a conventional optical microscope at $100\times$. This high-throughput nature provides an extra advantage to characterize several thousand cells within a single digital frame.

2.2 Preparation of Various Cell Lines

In this work we used various cell lines, starting from red blood cell (RBC), white blood cell (WBC), cancer cell lines HepG2 (human liver cell-line) and MCF7 (human breast cancer cell-line), and polystyrene microbeads of $10 \mu\text{m}$ and $20 \mu\text{m}$. The preparations of these cell lines are as follows [2, 3]. The use of human whole blood in the experiment was approved by the Institutional Review Board (Approval No. # 2021AN0040 of Korea University Anam Hospital (Seoul, Korea).

RBC: The RBC samples were prepared from the whole blood samples that were collected from the Korea University Anam Hospital under IRB approval. The samples were diluted about 16,000 times by using RPMI solution (Thermo Scientific, Waltham, MA, USA) [2, 3].

WBC: First, Ficoll solution (Ficoll-PaqueTM Plus, GE Healthcare, Chicago, IL, USA) was used to isolate mononuclear cells from the whole blood. The samples of peripheral blood mononuclear cells (PBMCs) obtained using the Ficoll solution are mixtures of lymphocytes and monocytes. To separate these two cell types, the MACS (Magnetic-activated cell sorting) device and antibodies (Miltenyi Biotec, Bergisch Gladbach, Germany) were utilized. The helper-T cells in the lymphocytes were separated using the CD4 antibody (#130-090-877), and the cytotoxic-T cells with the CD8 antibody (# 130-090-878). Finally, $10 \mu\text{L}$ of this solution was then loaded into the unruly C-Chip cell counting chamber [2, 3].

HepG2: The HepG2 cell lines were prepared from the American Type Culture Collection (ATCC HB-8065) and incubated in a high-glucose medium (DMEM, Merck, Darm-stadt, Germany) with 10% heat-inactivated fetal bovine serum, 0.1% gentamycin, and a 1 penicillin/streptomycin solution under 95% relative humidity and 5% CO_2 at 370°C . The developed cells were then trypsinized and separated from 24 well plate and incubated from 2–5 min at 370°C . These cells were then diluted with DMEM solution [2, 3].

MCF7: The MCF7 cell samples were prepared from the American Type Culture Collection (ATCC HTB-22). The cells were preserved in a solution of DMEM containing 1% penicillin/streptomycin solution, 0.1% gentamycin, and 10% calf serum at 95% relative humidity and 5% CO_2 at 370°C . These cells were then trypsinized and separated from the 24 well plate. These separated cells were then incubated for 2–5 min at 370°C . The cells were then washed with DMEM solution. $10 \mu\text{L}$ of this solution was then loaded in the C-Chip [2, 3].

Polystyrene microbead: The $10 \mu\text{m}$ and $20 \mu\text{m}$ bead samples were prepared by diluting the respective polystyrene microbeads (Thermo Scientific, Waltham, MA, USA) with de-ionized water [2, 3].

2.3 Dataset Creation

A whole frame LSIT image (of cell diffraction patterns) contains an average of ~ 500 diffraction patterns of microparticles. Deep learning-based architectures utilize the features of each class, and typically require a minimum of a few hundred diffraction patterns of each cell type for optimal learning. Therefore, we cropped individual diffraction patterns of each cell type (that were verified using a traditional microscope) with a window of 66×66 pixels as shown in Fig. 1d. This window size included the complete sample signature along with a minimal background that would provide complete cell-line information during the auto-feature selection process in learning algorithms. We further augment this base sample set by rotating the individual diffraction patterns with an increasing angle of 10 degrees clockwise. Finally, a dataset of 1980 samples for each of the 6 cell lines and microparticles was created, totaling 11,880 samples for all the classes under study. The typical architecture of a CNN is illustrated in Fig. 1e. As many learning algorithms are black-box models, it is difficult to ascertain the optimal cell-signal size that covers the majority of the information and minimal background. Naturally, a smaller cell-size would need lesser computation and have lesser noise. Hence, we created the dataset for 60×60 , 56×56 , 50×50 , 46×46 , 40×40 , and 36×36 cell sizes as input sets, with each set further divided into training and test folds. As the data augmentation used sample rotation, the splitting of the dataset into the train, validation, and test folds needs to be done while keeping a check on data leakage. Augmented samples distributed across the train and test sets may bias the model and may give a wrong estimate of its performance as the test data may not be of entirely “unseen” samples. Accounting for this, the 1980 samples of each class were carefully split into 1490 training samples, 166 validation samples, and 324 testing samples.

Though the cell-lines may seem visually similar, there are significant differences in the statistical distributions of the pixel illumination intensity in the cell diffraction pattern as revealed in our exploratory data analysis. The 2D contour plots (in Figure 2) show the observed variances. Hence, it is possible for intelligent algorithms to automatically identify and utilize the descriptive features in signal enhancement as well as classification.

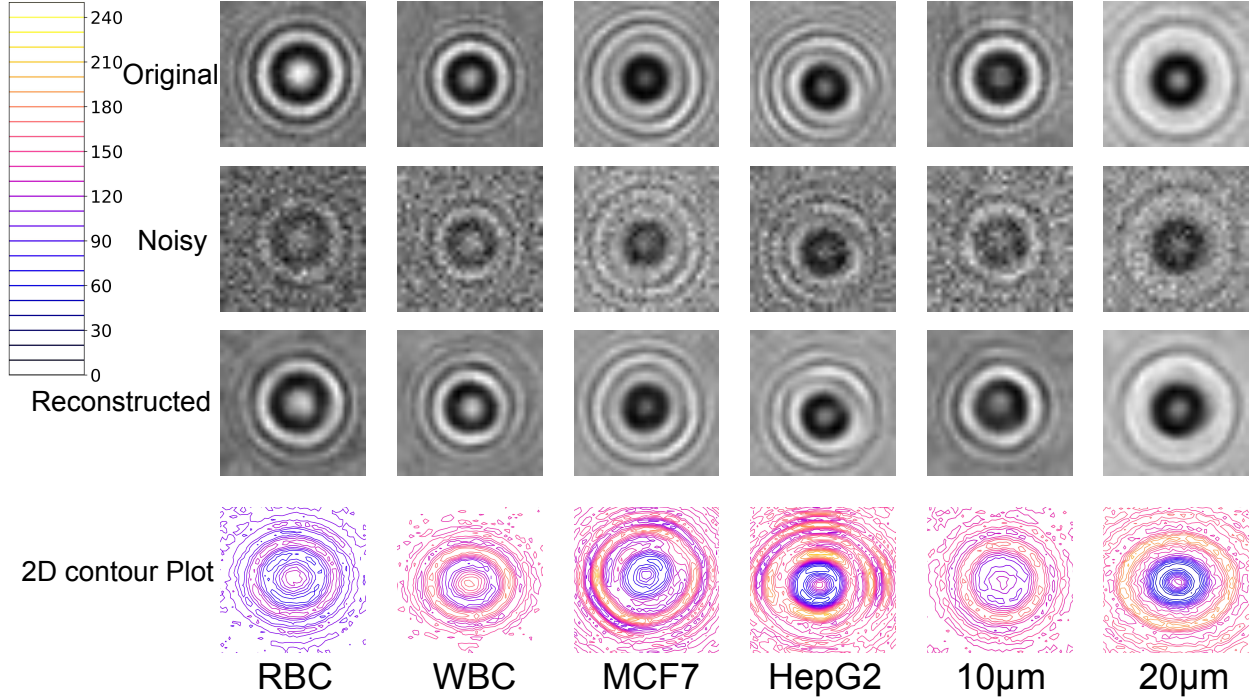


Figure 2: Reconstructed results from the optimized CNN. The top row is the original LSIT image (cell diffraction pattern) of a single RBC, WBC, MCF7, HepG2, $10 \mu\text{m}$ beam, and $20 \mu\text{m}$ bead. The second row is the noisy version (with variance 100) of the corresponding original images (cell diffraction pattern). The third row is the denoised version of the corresponding original images (cell diffraction pattern) from the noisy image (cell diffraction pattern). The fourth row is the 2D intensity contour plot of the original image (cell diffraction pattern) to show the unique signature of each of these cell lines.

2.4 Denoising Modality

For denoising of the LSIT micrographs, we adopted the concept of autoencoder [24]. An autoencoder is an unsupervised scheme that scuffles to recreate the input at its output. It consists of an input layer (x), an output layer (r), and a hidden layer (h). The hidden layer h termed as a code layer stands for the input in a revised dimension. The whole net-work structure can be labelled into two parts. The first part is an encoder, which tries to code the input as $h = f(x)$, and the second part is a decoder which tries to recreate the input from the reduced code layer as $r = g(h)$, where r is the recreated assortment of input x . Basically, it tries to attain $r = g(f(x))$. However, this is not a linear transformation since the model is enforced to learn the significant features of the input to encode it into the code layer.

In this work, we specifically used the denoising version of the autoencoder. Traditionally, the autoencoders try to reduce the loss as

$$L(x, g(f(x)))$$

. However, the denoising autoencoder attempts to reduce the cost as

$$L(x, g(f(x')))$$

where x' is the noisy form of the input x . And we tried two different methods to design the denoising architectures, namely, extreme learning machine (ELM) and convolutional neural network (CNN).

2.4.1 ELM

This is a single hidden layer fully connected architecture [25]. In this method, the input weights are initiated randomly and kept intact. Only the output weights take part in the learning process through a straightforward learning method [25, 26, 27]. For N arbitrary input samples $x_i \in R^n$ and their counterpart targets $t_i \in R^m$, the ELM achieves this mapping using the following relation as shown in Equation (1).

$$H\beta = T \quad (1)$$

Here, H is the hidden layer output matrix, β is the output weight matrix, i.e., between the hidden layer and the output layer, and T is the target matrix or matrix of desired out-put [26]. From Equation (1), we can obtain the β using Moore–Penrose pseudoinverse [25] as shown in Equation (2).

$$\beta = (H^T H)^{-1} H^T T \quad (2)$$

In the extended sequential learning form of ELM, the β can update sequentially. This provides an added advantage of updating the learning whenever a new type of sample is available, thus providing the flexibility of transfer of learning. The β update mechanism [28, 29] is as shown in Equation (3).

$$\beta_n = \beta_{n-1} + P_n^{-1} (T_n - H_n \beta_{n-1}) H_n^T \quad (3)$$

Here

$$P_n = P_{n-1} + H_n H_n^T \quad (4)$$

For $n = 1$,

$$P_{n-1} = P_0 = \left(\frac{1}{C} + H_0 H_0^T \right) \quad (5)$$

Here H_0 is the hidden layer output with the 1st sample or 1st batch of samples [30].

2.4.2 CNN

Convolutional neural networks (CNN) [6, 19, 20] are a type of neural network widely used in the analysis of spatial data such as image classification and object segmentation. In this network, two-dimensional kernels are used to extract the spatial features from the input patterns, using a convolution operation between the kernel and the input. The typical

architecture of a CNN is as shown in Fig. 1e. Here, the kernel is shared spatially by the input or by the feature map. The feature at the location (i, j) in the k^{th} feature map of the l^{th} layer can be evaluated as shown in Equation (6).

$$Z_{i,j,k}^l = (W_K^l)^T X_{i,j}^l + b_k^l \quad (6)$$

Here, W_K^l and b_k^l are the weights and the bias vector of the k^{th} filter in the l^{th} layer. Here the weight layer is shared spatially which reduces the complexity. $X_{i,j}^l$ is the value of the input at location (i, j) of the l^{th} layer. The nonlinearity in this network can be obtained by introducing the activation function, denoted here as $g(\cdot)$. The activated output can be represented as shown in Equation (7).

$$a_{i,j,k}^l = g(Z_{i,j,k}^l) \quad (7)$$

Additionally, there are pooling layers that introduce shift-invariance by reducing the resolution of the activated feature maps. Each pooling layer connects the feature map to the preceding convolutional layer. The expression for pooling is as shown in Equation (8).

$$y_{i,j,k}^l = P(a_{n,m,k}^l), \forall (m, n) \in R_{i,j} \quad (8)$$

Here $P(\cdot)$ is a pooling operation for the local neighborhood $R_{i,j}$ around the location (i, j) . In this work, we used CNN for both denoising as well as classification. The details of their architectures and their impacts are discussed in the result section.

3 Results and Discussion

3.1 Performance of Denoising Algorithms

For efficient and adaptive denoising, we analyzed various autoencoder schemes, starting with the fully-connected autoencoder. In our first iteration, we experimented with the fully connected network having three hidden layers with 512, 256, and 512 neurons, respectively. The input layer is the 1D vectorized array of the input cell diffraction pattern, e.g., of 66×66 pixels. The input to the model is the noisy version of the input cell diffraction pattern and the expected target output is the original cell diffraction pattern. The noisy cell diffraction patterns were created using a Gaussian distribution with variance ranging from 100 to 600 with zero mean (refer to the supplementary section (5) for detail). Further, we experimented with an increased network size having five hidden layers with 256, 128, 64, 128, and 256 neurons, respectively. In all these networks, rectified linear unit (ReLU) was used as the activation function while mean squared error (MSE) [31, 32, 33, 34] was used to calculate the loss. The Adam optimizer [35, 36] was found to deliver better convergence and hence used to perfect the weight and biases. The denoising performance was quantified in terms of the improvement in SNR, measured in dB, denoted here by SNR_{imp} , as given by Equation (9) [37].

$$SNR_{imp} = SNR_{out} - SNR_{in} \quad (9)$$

$$\text{where } SNR_{out} = 10 \log_{10} \frac{\sum_{n=1}^N x_i^2}{\sum_{n=1}^N (\hat{x}_i - x_i)^2} \quad \text{and} \quad SNR_{in} = 10 \log_{10} \frac{\sum_{n=1}^N x_i^2}{\sum_{n=1}^N (\tilde{x}_i - x_i)^2}$$

Here x_i is the value of sampling point i in the original LSIT signal, \tilde{x}_i is the value of sampling point i in the noisy LSIT, and \hat{x}_i is the value of sampling point i in the denoised version of the same cell diffraction pattern. N is the total number of sample points in that LSIT image (cell diffraction patterns).

The fully connected network for both the above configuration shows no significant improvement in SNR_{imp} after reaching saturation at around - 10.08 dB. For further improvement, we experimented with CNN architecture using various models with a different number of convolution layers and distinct kernel sizes. The configuration of the model which accomplished the best outcomes is $3 \times 3, 3 \times 3, 5 \times 5, 5 \times 5, 7 \times 7, 7 \times 7, 1 \times 1$ with 32 filters in each layer except the last layer. The last layer consists of a single pixel filter (1×1 filter) that is used to condense the output across all the 32 filters. Here, the input and output size are the same. Padding was used to maintain the original size after the output of each convolutional layer. Adam optimizer was used to optimize the network to reduce the mean squared error loss. The CNN results show a better reconstruction as shown in Figure 2.

Table 1: Comparison of improved SNR with respect to the variance for various denoising modalities (here we keep input and output size as 50×50)

Variance	Gaussian	Average	Median	Bilateral	BM3D	CNN	ELM
100	4.525580	4.237872	3.199475	-0.02635	5.684597	6.06905	5.79161
200	4.613044	4.198564	3.068866	-0.00640	5.713797	7.38544	6.31896
300	4.476552	4.259405	3.078091	-0.10943	5.119646	7.26487	6.57256
400	4.674922	4.703331	3.405470	-0.05448	3.792226	7.71265	6.36135
500	4.128021	4.201562	3.198964	-0.14542	2.206876	7.72364	6.09254
600	4.023621	4.183404	2.908946	-0.16924	1.683290	7.97877	6.19359

The CNN network has been optimized for various parameters. First, the optimization of the network for various design parameters, such as varying the convolution layers and the kernel sizes, was carried out. The results in Figure 3a show that the architecture with kernel sizes 3×3 , 3×3 , 5×5 , 5×5 , 7×7 , 7×7 , 1×1 has a better performance in terms of SNR_{imp} . The performance of the optimized network for various noise parameters, as shown in Figure 3b, indicates the network performs better reconstruction with increasing noise variance in the image (cell diffraction pattern). An increase in the variance results in a noisier image (cell diffraction pattern), which warrants a detailed reconstruction to reverse it to the original form, and hence larger the value of SNR_{imp} . Therefore, a higher improvement in SNR_{imp} implies the network has learned the optimal representational features for the cell types which enables it to perform a better qualitative reconstruction. Fig. 3c compares the reconstruction performance of the model on different sizes of the input image (cell diffraction pattern). Due to the black-box nature of deep learning methods, we had to create datasets with multiple cell-signature dimensions, such that the smallest size just covered the central signature of the cell and increased the window size till it covered a significant background portion as well. The models were evaluated across varying cell sizes to determine the optimal signal to background ratio, the spatial extent up to which the models covered the features, and to study its effects on the model performance. This analysis is critical in understanding the model explainability and interpretability since having a size larger than the optimum increases the inclusion of background artifacts that affect denoising as well as overpower the cell signal while having a smaller one could exclude the important deterministic features of the cell signature. The convergence in the training phase of the network is as shown in Figure 3d. The results depict the loss across the first epoch, with a high variation in the initial phase, gets smoother towards the end of the first iteration. The advantage of this system is that it generalizes well for all cell lines using the same model.

Further, we tried the ELM architecture which is well known for its fast convergence [25]. The results in Figure 3e–h show the performance of the ELM architecture with varying number of neurons in the hidden layer. As it can be concluded from Figure 3e, the model with 2000 neurons provides better performance in terms of SNR_{imp} . Further, the optimized model has been used to test the performance across various noise levels as shown in Figure 3f. It is observed that the model maintains the SNR_{imp} value on increasing the noise in the input image (cell diffraction pattern), i.e., the image (cell diffraction pattern) quality of the output relative to the input remains the same. The results of the model performance across different sizes of the input image (cell diffraction pattern), as shown in Figure 3g, indicate that the 40×40 is having a higher value of SNR. However, the variation is of 2 as compared to the variation for the size 50×50 , that is of 1.5, which is the lowest compared to all the other sizes. Since CNN shows a substantial performance with lower variance for the 50×50 input size, therefore, we fixed it as optimal for all the further studies and comparisons. Figure 3h shows the loss across the first epoch for ELM which is remarkably high initially but converges faster, as compared to CNN, after training with only a few thousand samples. This faster convergence may help save time and resources during incremental training phases for newer cell types. The performances of these optimized models have been compared with the traditional denoising methods as shown in Table 1 (The comparative visual reconstructions are provided in the supplementary document (Section 5)). It is concluded from the data that CNN shows better performance compared to the other modalities (The details of the traditional methods are provided in the supplementary document (Section 5)). Therefore, we prefer to use CNN for denoising.

3.2 Performance of Classification Algorithm

Since the diffraction patterns of cells and microparticles in a LSIT micrograph depend upon their physical and optical properties, therefore, the diffraction patterns carry the unique signatures of each of the cell types as shown in the 2D contour plot in Figure 2. These unique signatures can be utilized for the classification of these cell types. Since our previous inference concludes that CNN works better for denoising, therefore we experimented with the same modality for the classification as well. In this work, in order to determine the optimal architecture of CNN for cell-line recognition, we first proceeded to find the optimal depth of the network by studying the classification performance of the model on increasing the depth, by adding convolutional and pooling layers, as well as by varying number of kernels

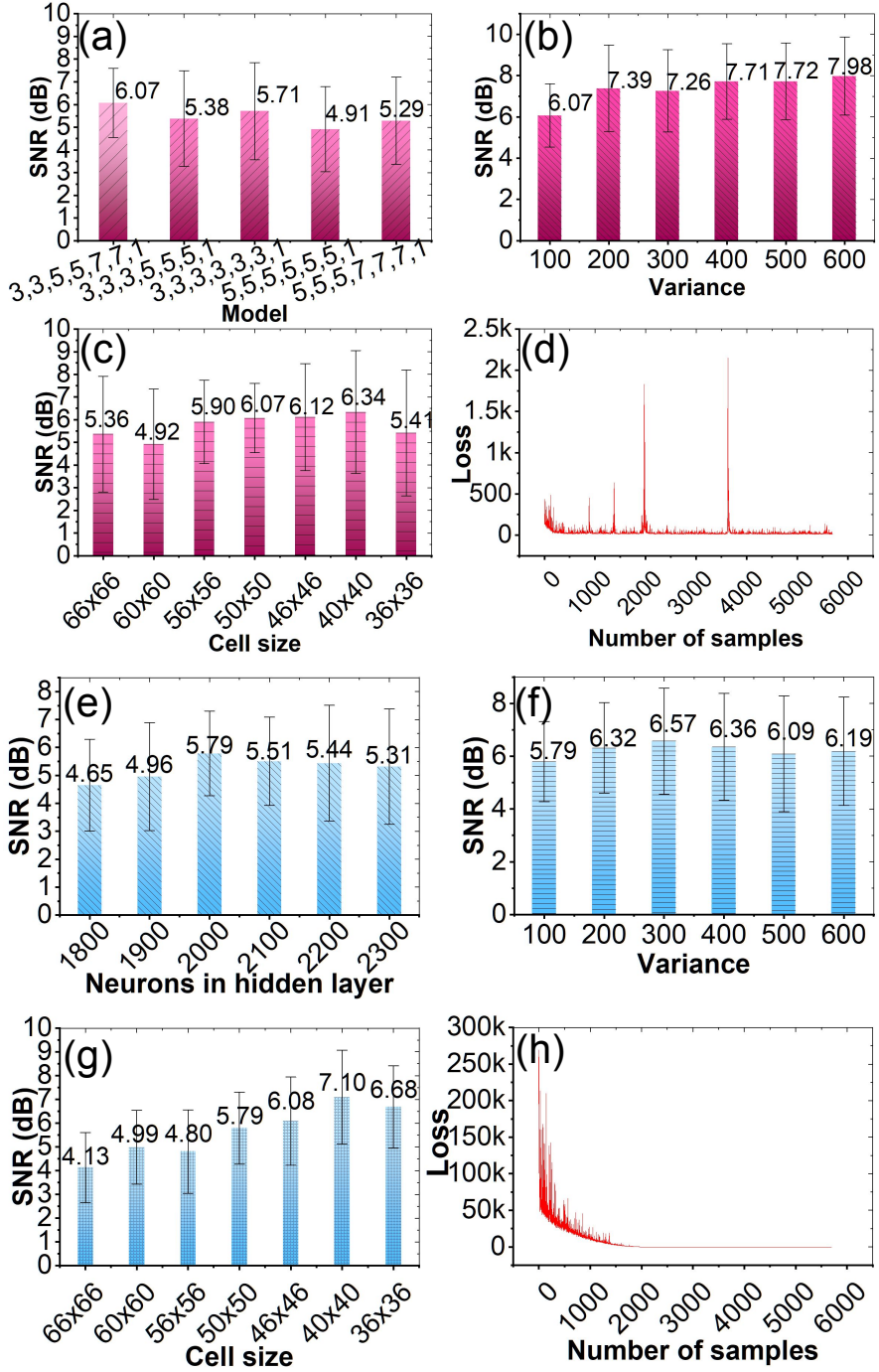


Figure 3: Results from the CNN and ELM autoencoder. (a) The performance of the CNN autoencoder for improved SNR (average of all the classes) across various layers and kernel sizes. (b) The performance of the CNN autoencoder across varying noise levels. Here, the variance of the Gaussian noise ranges from 100 to 600, and is evaluated on the optimal network architecture, i.e., 3,3,5,5,7,7,1. (c) The performance of the CNN autoencoder across various input sizes (cropping size). Here, the sizes vary from 66×66 to 36×36 . (d) The convergence of the optimal CNN network with the number of samples for the first epoch. (e) The number of hidden layer neurons in ELM autoencoder vs. improvement in SNR, (f) Variance vs. improved SNR for ELM autoencoder, (g) Input size vs. improved SNR for ELM autoencoder, and (h) The convergence of ELM autoencoder within the 1st epoch.

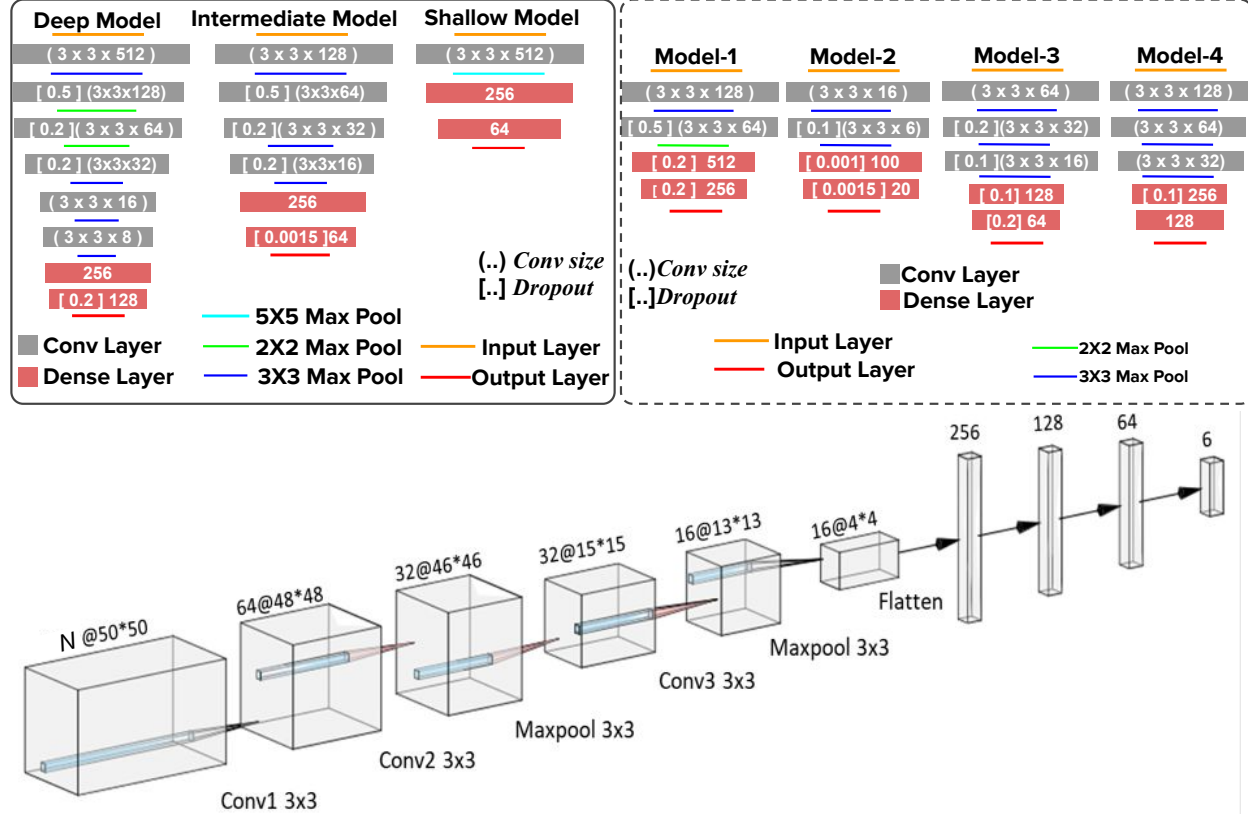


Figure 4: The CNN Architectures with varying depth. The models in the solid box are for the optimization of the model with varying depth. The models inside the dotted box are for the optimization of the parameters. Here, the orange line is the input layer and the rectangle represents the 2D convolution layer. The kernel size and number of kernels are indicated inside the round brackets, the dropout rate in square brackets, and the number of neurons in fully connected layers are placed directly within the rectangle. The aqua blue, green, and purple lines are the max-pool layers. The red line is the output layer and uses a SoftMax activation function. The final optimized architecture is as represented by the last 3D figure.

and kernel size, till we reached performance saturation. We have experimented with and evaluated various shallow and deep CNN models to classify cell lines. The details of the model architecture are as described in Figure 4.

The Deep Model starts with a convolutional (Conv2D) layer having 512 kernels of size 3×3 , followed by a max-pooling layer of same kernel size. The output from this is further convoluted with 128 kernels of 3×3 size with a dropout rate of 0.5, and then a max pool with 2×2 kernel. This output goes to a Conv2D layer with 64 of 3×3 sized kernels and a dropout rate of 0.2. We further reduce the dimension using a 2×2 max pool kernel. The output of this layer further convolves with 32 of 3×3 kernels, then a dropout of 0.2. The output dimension from this convoluted layer is further reduced by using the max pool with a 3×3 kernel. This again convolves with 16 of 3×3 kernels, and a max pool layer with 3×3 kernel. The output of which is again convoluted with 8 of 3×3 kernels, followed by a 3×3 max pool. This output is then vectorized and input to a fully connected (FC) layer having 256 nodes, and then to another FC with 128 nodes and having a dropout of 0.2. The final layer is a SoftMax function, with 6 output nodes. The model architectures used for studying the impact of the network depth and breadth on performance are well described in Figure 4. Once the approximate optimal depth and breadth had been determined, we proceeded to fine-tune the hyper-parameters such as the number of kernels, kernel size, and dropouts, to reach the best performance of the models across varying cell sizes, i.e., input dimension of cells. In all the models, Adam [38] provided better convergence as compared to other optimizers and has been used as the model optimizer, with categorical cross-entropy [39, 40] as a loss estimator. The result for depth and breadth optimization indicates that the average accuracy of the intermediate model is >0.85 (including all the classes), whereas it is <0.85 for shallow and deep networks. Therefore, we proceed with this intermediate model as an optimum model for further study. Considering the intermediate model has the optimum breadth and depth, the further optimization of the parameters and the results are as shown in Figure 5a.

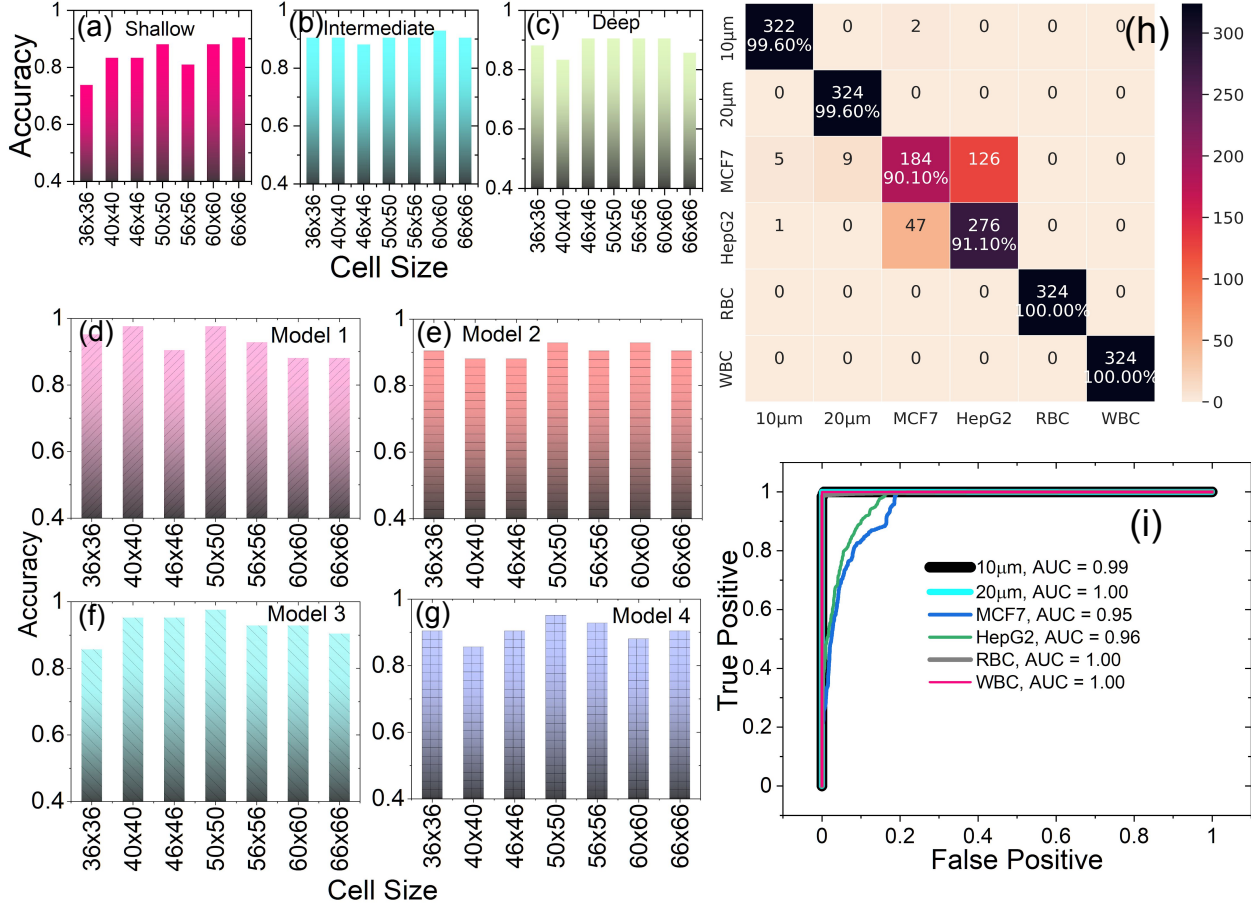


Figure 5: Results for the optimization of the CNN model. (a) Performance of the fine-tuned intermediate architecture. (b) The confusion matrix showing classification accuracy on the test dataset across all cell lines using the fine-tuned and optimized model. (c) The receiver operating characteristic (ROC) curve for each of the cell lines for the optimized model.

From Figure 5a, it is inferred that Model 3 shows better classification performance, on the validation fold, of all models. The results depict that there is consistency in performance for the input sizes 40x40 to 66x66, with a very small variance in the accuracy. The performance of this optimized model is further evaluated over the test dataset containing 324 samples of each cell type. The per-class performance of this model is shown in the confusion matrix of Figure 5b. The results depict that the model can classify RBC, WBC, 10 μ m, and 20 μ m bead with over 99% accuracy. However, the comparatively poor performance of about 90% for the cancer cells, HepG2 and MCF7, can be attributed to the non-homogeneity in their signature characteristics as well as the lack of sufficient original samples which further complicates the issue. This is well depicted in our previous work [4] (see Figure 2 of the reference). From the receiver operating characteristic (ROC) curve for all the cell lines shown in Figure 5c, the area under the curve (AUC) for all the cell lines is >0.99 , except MCF7 (~ 0.95) and HepG2 (~ 0.96). From these results, it can be inferred that the classifier is working well, especially for RBC, WBC, 10 μ m, and 20 μ m beads. The visualization of the internal activation maps, as shown in the supplementary (Section 5), implies that the network is learning core descriptive features in the diffraction signatures rather than using some random feature.

The performance evaluation of the proposed AI model with various matrices such as true positive (TP), true negative (TN), false positive (FP), false negative (FN), accuracy, recall, specificity, sensitivity, F1 score, positive predictive value (PPV) and negative predictive value (NPV) is summarized in Table 2.

Additionally, we also investigate the transfer of learning to gauge the ability of the trained network to adapt to newer cell types (Figure 6). For this scenario, the CNN was initially trained with all the cell lines except RBC. From the epoch versus accuracy graph in Figure 6a, the transfer training achieved higher accuracy with the same number of epochs compared to the initial training. This is also validated by the epoch versus loss graph in Figure 6b. From these results, it

Table 2: Performance evaluation scores of the proposed AI model using various metrics for different cell types

Sample Type	TP	TN	FP	FN	Accuracy	Precision	Recall	Specificity	Sensitivity	F1	PPV	NPV
10 μ m bead	322	1614	2	6	0.9959	0.9938	0.9817	0.9988	0.9817	0.9877	0.9938	0.9963
20 μ m bead	324	1611	0	9	0.9954	1.0000	0.9730	1.0000	0.9730	0.9863	1.0000	0.9944
MCF7	184	1571	140	49	0.9028	0.5679	0.7897	0.9182	0.7897	0.6607	0.5679	0.9698
HepG2	276	1494	48	126	0.9105	0.8519	0.6866	0.9689	0.6866	0.7603	0.8519	0.9222
RBC	324	1620	0	0	1.0000	1.0000	1.0000	1.0000	1.0000	1.0000	1.0000	1.0000
WBC	324	1620	0	0	1.0000	1.0000	1.0000	1.0000	1.0000	1.0000	1.0000	1.0000

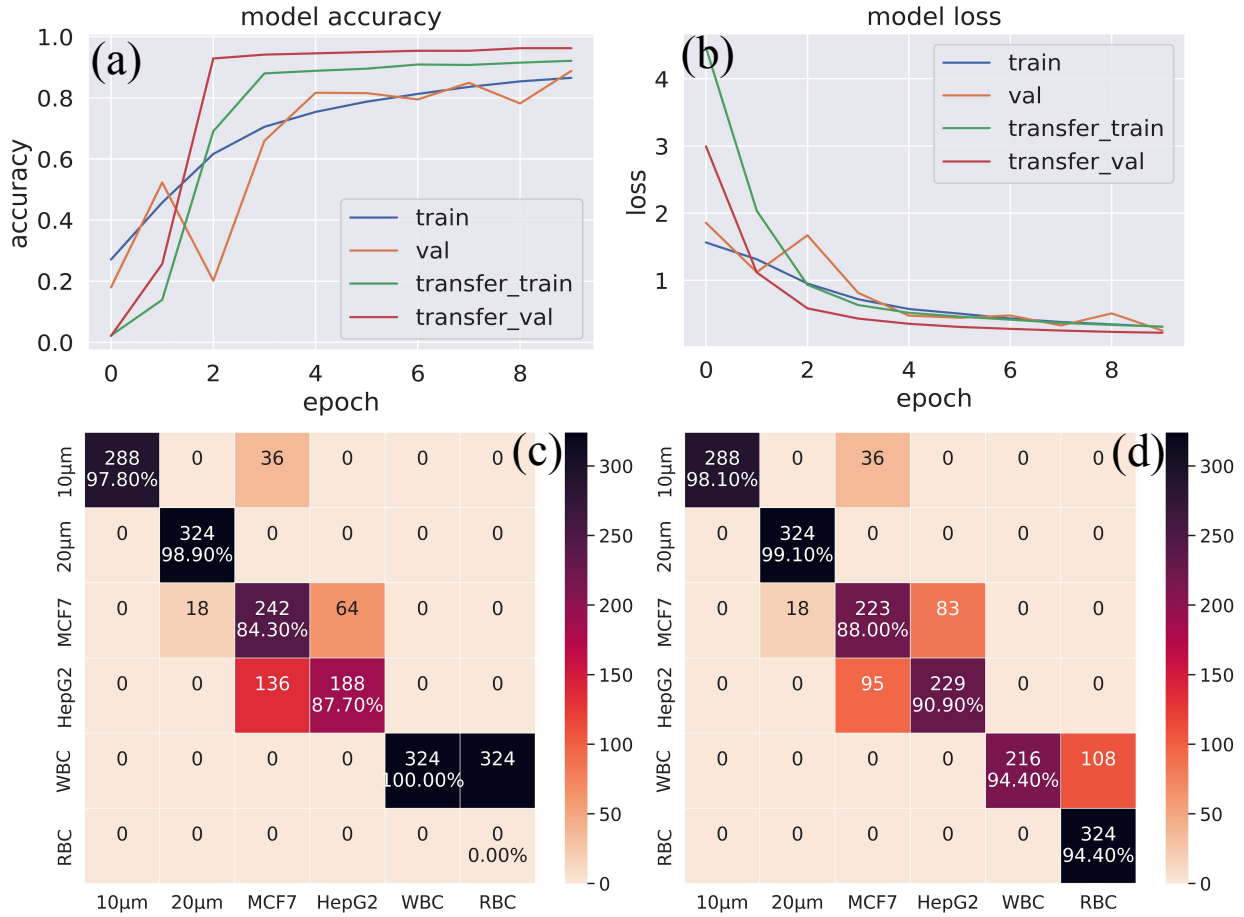


Figure 6: The results from the transfer of learning study. (a) epoch vs. accuracy graph for the initial epochs in the initial training phase without RBC and then the transfer of training with RBC. The blue and saffron colors represent the initial training accuracy and validation curves. The green and red lines represent the transfer learning accuracy and validation curves, (b) epoch vs. loss, (c) the confusion matrix from the pre-trained model, (d) the confusion matrix with the re-trained model.

can be inferred that the network can be effectively used to adapt to newer cell lines with very less amount of training. From the per-class test accuracy shown in Figure 6c, it is observed that the model misclassified all the RBC samples as WBC. In the transfer of the learning phase, the initially trained network is frozen except for the last layer, which is modified to accommodate the newer class and kept trainable. The network is then re-trained with a mix of RBC samples. The per-class test accuracy of the re-trained model is shown in the confusion matrix of Figure 6d, where it is inferred that the re-trained network can classify RBC correctly with substantial accuracy.

The comparison between the proposed AI method and the manual method for counting various cell types from a heterogeneous sample is shown in Figure 7. This comparison shows the robustness of the model.

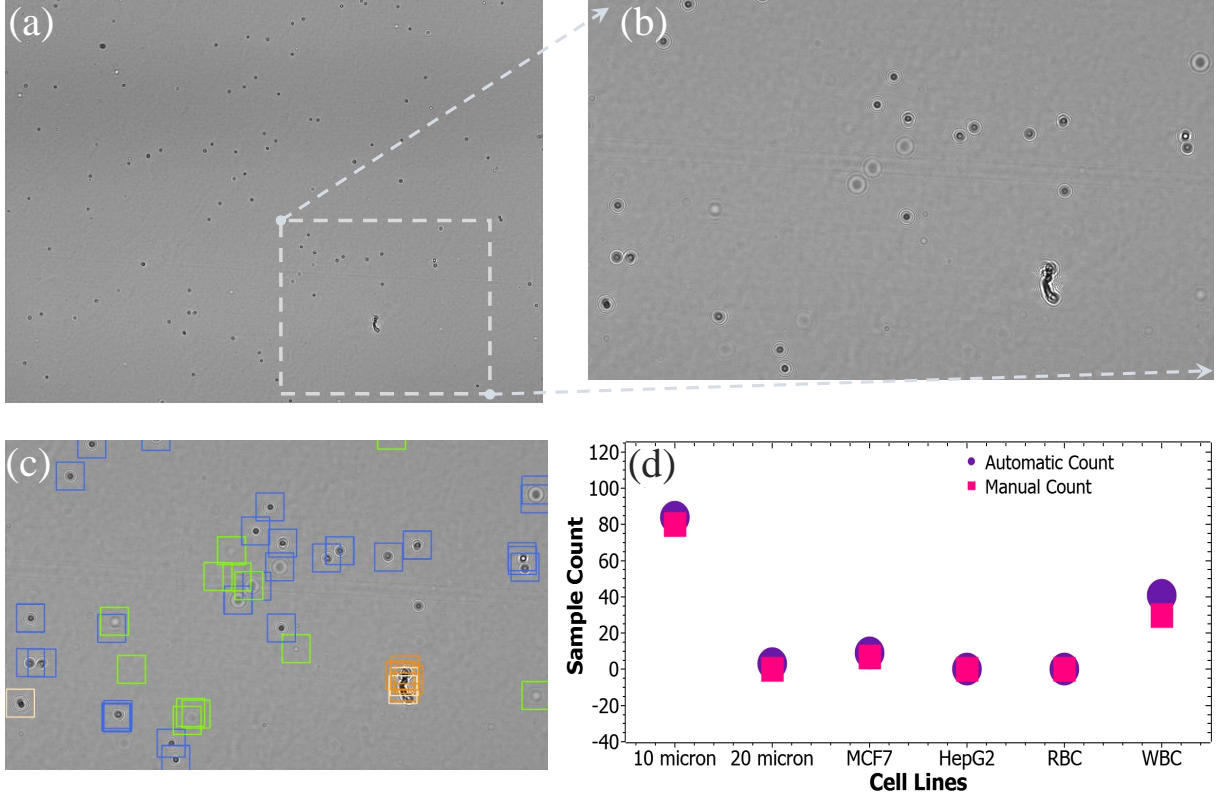


Figure 7: Comparison between the proposed AI method and the manual method for counting. (a) A whole frame LSIT micrograph, (b) magnified region-of-interest (ROI) of the whole frame LSIT micrograph, (c) automatically classified cell diffraction patterns of the ROI, and (d) comparison of the cell counts between those two different modalities.

4 Conclusion

In conclusion, we have explored the advantage of neural networks in the characterization of LSIT micrographs. Here, we have perfected neural networks that can automatically improve the signal quality and classify the cell types. We find that this neural network can classify the RBC, WBC with great accuracy, i.e., over 98%, and the cancer cell with an accuracy of about 90%. This network is also flexible for adapting to newer cell lines by retraining the trained network with very few samples. Together with this algorithm, the lightweight and cost-effective LSIT setup can be utilized as a point of care system for the diagnosis of pathological disorders in the resource-limited setup of our world. In our future work, we aim to combine the denoising and classification modalities due to the significant overlap in their operation. This will remove the dual training times as well as minimize computation costs. Also, we aim to work on improving their performance and deploying it in real scenarios.

Acknowledgments

Funding: M.R. acknowledges the seed grant No. ORSP/R&D/PDPU/2019/MR/RO051 of PDPU (the AI software development part) and the core research grant No. CRG/2020/000869 of the Science and Engineering Research Board (SERB), India. S.S. acknowledges the support of the Basic Science Research Program (Grant#: 2014R1A6A1030732, Grant#: 2020R1A2C1012109) through the National Research Foundation (NRF) of Korea, the Korea Medical Device Development Fund (Project#: 202012E04) granted by the Korean government (the Ministry of Science and ICT, the Ministry of Trade, Industry and Energy, the Ministry of Health & Welfare, the Ministry of Food and Drug Safety), and the project titled ‘Development of Management Technology for HNS Accident’ and ‘Development of Technology for

Impact Assessment and Management of HNS discharged from Marine Industrial Facilities', funded by the Ministry of Oceans and Fisheries of Korea.

Institutional Review Board Statement: All human blood samples were approved by the Institutional Review Board of Anam Hospital, Korea University (# 2021AN0040).

References

- [1] Onur Mudanyali, Anthony Erlinger, Sungkyu Seo, Ting Wei Su, Derek Tseng, and Aydogan Ozcan. Lensless on-chip imaging of cells provides a new tool for high-throughput cell-biology and medical diagnostics. *Journal of Visualized Experiments*, 34(34):e1650, 2010.
- [2] Mohendra Roy, Dongmin Seo, Chang-Hyun Hyun Oh, Myung-Hyun Hyun Nam, Young Jun Kim, and Sungkyu Seo. Low-cost telemedicine device performing cell and particle size measurement based on lens-free shadow imaging technology. *Biosensors and Bioelectronics*, 67:715–723, 2015.
- [3] Mohendra Roy, Geonsoo Jin, Dongmin Seo, Myung Hyun Nam, and Sungkyu Seo. A simple and low-cost device performing blood cell counting based on lens-free shadow imaging technique. *Sensors and Actuators, B: Chemical*, 201:321–328, 2014.
- [4] Mohendra Roy, Dongmin Seo, Sangwoo Oh, Yeonghun Chae, Myung Hyun Nam, and Sungkyu Seo. Automated micro-object detection for mobile diagnostics using lens-free imaging technology. *Diagnostics*, 6(2):17, 2016.
- [5] Mohendra Roy, Geonsoo Jin, Jeong Hoon Pan, Dongmin Seo, Yongha Hwang, Sangwoo Oh, Moonjin Lee, Young Jun Kim, and Sungkyu Seo. Staining-free cell viability measurement technique using lens-free shadow imaging platform. *Sensors and Actuators, B: Chemical*, 224:577–583, 2015.
- [6] Yun Liu, Krishna Gadepalli, Mohammad Norouzi, George E. Dahl, Timo Kohlberger, Aleksey Boyko, Subhashini Venugopalan, Aleksei Timofeev, Philip Q. Nelson, Greg S. Corrado, Jason D. Hipp, Lily Peng, and Martin C. Stumpe. Detecting Cancer Metastases on Gigapixel Pathology Images. *CoRR*, mar 2017.
- [7] Kun Hsing Yu, Andrew L. Beam, and Isaac S. Kohane. Artificial intelligence in healthcare, oct 2018.
- [8] Yun Liu, Timo Kohlberger, Mohammad Norouzi, George E. Dahl, Jenny L. Smith, Arash Mohtashamian, Niels Olson, Lily H. Peng, Jason D. Hipp, and Martin C. Stumpe. Artificial intelligence-based breast cancer nodal metastasis detection insights into the black box for pathologists. *Archives of Pathology and Laboratory Medicine*, 143(7):859–868, oct 2019.
- [9] Diego Ardila, Atilla P. Kiraly, Sujeeth Bharadwaj, Bokyung Choi, Joshua J. Reicher, Lily Peng, Daniel Tse, Mozziyar Etemadi, Wenxing Ye, Greg Corrado, David P. Naidich, and Shravya Shetty. End-to-end lung cancer screening with three-dimensional deep learning on low-dose chest computed tomography. *Nature Medicine*, 25(6):954–961, jun 2019.
- [10] Hyungsoon Im, Divya Pathania, Philip J. McFarland, Aliyah R. Sohani, Ismail Degani, Matthew Allen, Benjamin Coble, Aoife Kilcoyne, Seonki Hong, Lucas Rohrer, Jeremy S. Abramson, Scott Dryden-Peterson, Lioubov Fexon, Misha Pivovarov, Bruce Chabner, Hakho Lee, Cesar M. Castro, and Ralph Weissleder. Design and clinical validation of a point-of-care device for the diagnosis of lymphoma via contrast-enhanced microholography and machine learning. *Nature Biomedical Engineering*, 2(9):666–674, sep 2018.
- [11] Pu Wang, Xiao Xiao, Jeremy R. Glissen Brown, Tyler M. Berzin, Mengtian Tu, Fei Xiong, Xiao Hu, Peixi Liu, Yan Song, Di Zhang, Xue Yang, Liangping Li, Jiong He, Xin Yi, Jingjia Liu, and Xiaogang Liu. Development and validation of a deep-learning algorithm for the detection of polyps during colonoscopy. *Nature Biomedical Engineering*, 2(10):741–748, oct 2018.
- [12] Zachary S. Ballard, Hyou Arm Joung, Artem Goncharov, Jesse Liang, Karina Nugroho, Dino Di Carlo, Omai B. Garner, and Aydogan Ozcan. Deep learning-enabled point-of-care sensing using multiplexed paper-based sensors. *npj Digital Medicine*, 3(1):1–8, dec 2020.
- [13] Yair Rivenson, Zoltán Göröcs, Harun Güneydin, Yibo Zhang, Hongda Wang, and Aydogan Ozcan. Deep learning microscopy. *Optica*, 4(11):1437, nov 2017.
- [14] Aydogan Ozcan. Deep learning-enabled holography (Conference Presentation). In Natan T. Shaked and Oliver Hayden, editors, *Label-free Biomedical Imaging and Sensing (LBIS) 2020*, volume 11251, page 60. SPIE, mar 2020.
- [15] Hongda Wang, Hatice C. Koydemir, Yunzhe Qiu, Bijie Bai, Yibo Zhang, Yiyin Jin, Sabiha Tok, Enis C. Yilmaz, Esin Gumustekin, Yilin Luo, Yair Rivenson, and Aydogan Ozcan. Deep learning enables high-throughput early detection and classification of bacterial colonies using time-lapse coherent imaging (Conference Presentation). In

David Levitz and Aydogan Ozcan, editors, *Optics and Biophotonics in Low-Resource Settings VI*, volume 11230, page 13. SPIE, mar 2020.

[16] Kevin de Haan, Tairan Liu, Yair Rivenson, Zhensong Wei, Xin Zeng, Yibo Zhang, and Aydogan Ozcan. Enhancing resolution in coherent microscopy using deep learning (Conference Presentation). In Gabriel Popescu, YongKeun Park, and Yang Liu, editors, *Quantitative Phase Imaging VI*, volume 11249, page 3. SPIE, mar 2020.

[17] Tairan Liu, Kevin de Haan, Bijie Bai, Yair Rivenson, Yi Luo, Hongda Wang, David Karalli, Hongxiang Fu, Yibo Zhang, John FitzGerald, and Aydogan Ozcan. Deep learning-based holographic polarization microscopy. *ACS Photonics*, 7(11):3023–3034, jul 2020.

[18] Seshadri Sastry Kunapuli, Praveen Chakravarthy Bh, and Upasana Singh. Enhanced Medical Image De-noising Using Auto Encoders and MLP. In *Communications in Computer and Information Science*, volume 932, pages 3–15. Springer Verlag, oct 2019.

[19] Sakshi Indolia, Anil Kumar Goswami, S. P. Mishra, and Pooja Asopa. Conceptual Understanding of Convolutional Neural Network- A Deep Learning Approach. In *Procedia Computer Science*, volume 132, pages 679–688. Elsevier B.V., jan 2018.

[20] Rikiya Yamashita, Mizuho Nishio, Richard Kinh Gian Do, and Kaori Togashi. Convolutional neural networks: an overview and application in radiology, aug 2018.

[21] Sungkyu Seo, Ting Wei Su, Derek K. Tseng, Anthony Erlinger, and Aydogan Ozcan. Lensfree holographic imaging for on-chip cytometry and diagnostics. *Lab on a Chip*, 9(6):777–787, mar 2009.

[22] Onur Mudanyali, Derek Tseng, Chulwoo Oh, Serhan O. Isikman, Ikbal Sencan, Waheb Bishara, Cetin Oztoprak, Sungkyu Seo, Bahar Khademhosseini, and Aydogan Ozcan. Compact, light-weight and cost-effective microscope based on lensless incoherent holography for telemedicine applications. *Lab on a Chip*, 10(11):1417–1428, 2010.

[23] Geonsoo Jin, In Hwa Yoo, Seung Pil Pack, Ji Woon Yang, Un Hwan Ha, Se Hwan Paek, and Sungkyu Seo. Lens-free shadow image based high-throughput continuous cell monitoring technique. *Biosensors and Bioelectronics*, 38(1):126–131, 2012.

[24] Pascal Vincent, Hugo Larochelle, Isabelle Lajoie, Yoshua Bengio, and Pierre Antoine Manzagol. Stacked denoising autoencoders: Learning Useful Representations in a Deep Network with a Local Denoising Criterion. *Journal of Machine Learning Research*, 11:3371–3408, dec 2010.

[25] Erik Cambria, Guang Bin Huang, Liyanaarachchi Lekamalage Chamara Kasun, Hongming Zhou, Chi Man Vong, Jiarun Lin, Jianping Yin, Zhiping Cai, Qiang Liu, Kuan Li, Victor C.M. Leung, Liang Feng, Yew Soon Ong, Meng Hiot Lim, Anton Akusok, Amaury Lendasse, Francesco Corona, Rui Nian, Yoan Miche, Paolo Gastaldo, Rodolfo Zunino, Sergio Decherchi, Xuefeng Yang, Kezhi Mao, Beom Seok Oh, Jehyoung Jeon, Kar Ann Toh, Andrew Beng Jin Teoh, Jaihie Kim, Hanchao Yu, Yiqiang Chen, and Junfa Liu. Extreme learning machines, 2013.

[26] Mihai Bucurica, Radu Dogaru, and Ioana Dogaru. A comparison of Extreme Learning Machine and Support Vector Machine classifiers. In *Proceedings - 2015 IEEE 11th International Conference on Intelligent Computer Communication and Processing, ICCP 2015*, pages 471–474, sep 2015.

[27] Gao Huang, Guang Bin Huang, Shiji Song, and Keyou You. Trends in extreme learning machines: A review, 2015.

[28] Nan Ying Liang, Guang Bin Huang, P. Saratchandran, and N. Sundararajan. A fast and accurate online sequential learning algorithm for feedforward networks. *IEEE Transactions on Neural Networks*, 17(6):1411–1423, nov 2006.

[29] André van Schaik and Jonathan Tapson. Online and adaptive pseudoinverse solutions for ELM weights. *Neurocomputing*, 149(Part A):233–238, 2015.

[30] Mohendra Roy, Sumon Kumar Bose, Bapi Kar, Pradeep Kumar Gopalakrishnan, and Arindam Basu. A Stacked Autoencoder Neural Network based Automated Feature Extraction Method for Anomaly detection in On-line Condition Monitoring. In *Proceedings of the 2018 IEEE Symposium Series on Computational Intelligence, SSCI 2018*, pages 1501–1507. Institute of Electrical and Electronics Engineers Inc., jan 2019.

[31] Farid E. Ahmed. Artificial neural networks for diagnosis and survival prediction in colon cancer, aug 2005.

[32] Yu Dong Zhang, Chichun Pan, Xianqing Chen, and Fubin Wang. Abnormal breast identification by nine-layer convolutional neural network with parametric rectified linear unit and rank-based stochastic pooling. *Journal of Computational Science*, 27:57–68, jul 2018.

[33] Khushboo Munir, Hassan Elahi, Afsheen Ayub, Fabrizio Frezza, and Antonello Rizzi. Cancer diagnosis using deep learning: A bibliographic review. *Cancers*, 11(9), sep 2019.

- [34] P. B. Shanthi, Faraz Faruqi, K. S. Hareesha, and Ranjini Kudva. Deep Convolution Neural Network for malignancy detection and classification in microscopic uterine cervix cell images. *Asian Pacific Journal of Cancer Prevention*, 20(11):3447–3456, 2019.
- [35] Li Shen, Laurie R. Margolies, Joseph H. Rothstein, Eugene Fluder, Russell McBride, and Weiva Sieh. Deep Learning to Improve Breast Cancer Detection on Screening Mammography. *Scientific Reports*, 9(1):1–12, dec 2019.
- [36] Diederik P. Kingma and Jimmy Lei Ba. Adam: A method for stochastic optimization. In *3rd International Conference on Learning Representations, ICLR 2015 - Conference Track Proceedings*. International Conference on Learning Representations, ICLR, dec 2015.
- [37] Hsin Tien Chiang, Yi Yen Hsieh, Szu Wei Fu, Kuo Hsuan Hung, Yu Tsao, and Shao Yi Chien. Noise Reduction in ECG Signals Using Fully Convolutional Denoising Autoencoders. *IEEE Access*, 7:60806–60813, 2019.
- [38] Yixiang Wang, Jiqiang Liu, Jelena Misic, Vojislav B. Misic, Shaohua Lv, and Xiaolin Chang. Assessing Optimizer Impact on DNN Model Sensitivity to Adversarial Examples. *IEEE Access*, 7:152766–152776, 2019.
- [39] Long Zhang, Hong Jie Gao, Jianhua Zhang, and Benjamin Badami. Optimization of the Convolutional Neural Networks for Automatic Detection of Skin Cancer. *Open Medicine (Poland)*, 15(1):27–37, jan 2020.
- [40] Łukasz Rączkowski, Marcin Możejko, Joanna Zambonelli, and Ewa Szczurek. ARA: accurate, reliable and active histopathological image classification framework with Bayesian deep learning. *Scientific Reports*, 9(1):1–12, dec 2019.

5 Supplementary Information

5.1 Convolutional Neural Network (CNN) workflow

Network Architecture	Output dimensions
0-Input	: N, 50x50 (batch size, input image)
1-Conv2D	: 64, 3x3, 48x48, Relu
2-Conv2D	: 32, 3x3, 46x46, Relu
3-MaxPool2D	: 32, 3x3, 15x15
4-Conv2D	: 16, 3x3, 13x13, Relu
5-MaxPool2D	: 16, 3x3, 4x4
6-Flatten	: 16, 4x4, 256
7-FC	: 128, Relu
8-FC	: 64, Relu
9-FC	: 6, Softmax

Here, FC represents Fully Connected layers in the CNN architecture.

Forward Propagation

Step1:

Given an input image I (50x50 single grayscale image) to be convolved with l^p kernels, the 2D convolution operation C is defined as

$$C_p^1 = f(I * k_{1,p}^1 + b_p^1) \text{ for } p=1 \text{ to } 64$$

where for $k_{1,p}^1$: “1” in the superscript denotes the hierarchical order of the convolution operation and $(1,p)$ in the subscript denotes 1 input channel, p^{th} output channel

b_p^1 represents the bias corresponding to each of the p kernels

* represents the convolution (element-wise product followed by addition) between the input and the kernel

f represents Relu activation, applied to the output of the convolution operation

Step2 :

$$C_q^2 = f(\sum_p C_p^1 * k_{p,q}^2 + b_q^2) \text{ for } p = 1 \text{ to } 64; q = 1 \text{ to } 32$$

Step3 :

$$M_q^1(i, j) = \max(C_q^2[3(i-1) + 1 : 3(i-1) + 3, 3(j-1) + 1 : 3(j-1) + 3]) \text{ for } i, j = 1 \text{ to } 1; q = 1 \text{ to } 32;$$

Step4 :

$$C_r^3 = f(\sum_q M_q^1 * k_{q,r}^3 + b_r^3) \text{ for } q = 1 \text{ to } 32; r = 1 \text{ to } 16$$

Step5 :

$$M_r^2(i, j) = \max(C_r^3[3(i-1) + 1 : 3(i-1) + 3, 3(j-1) + 1 : 3(j-1) + 3]) \text{ for } i, j = 1 \text{ to } 4; r = 1 \text{ to } 16;$$

Step6 :

$$g = G(\{M_r^2\}; r=1 \text{ to } 4); \text{ (flatten/vectorization)}$$

The rest of the steps for the fully connected layers are the same as in Feedforward Multi-Layer Perceptron (MLP).

Backward Propagation

Let L be the loss at the end of the epoch during the training phase.

All the equations for backpropagation for the fully connected layers are the same as in MLP till the FC-7 layer.

Step1:

Those computed gradients from layer FC-7 simply need to be vectorized into matrix 4x4x16.

Reshape output error vector Δg (256x1) into (4x4x16):

$$\{\Delta M_r^2\}_{r=1 \text{ to } 4} = G^{-1}(\Delta g); \text{ (flatten/vectorization)}$$

Since it is a max-pool operation, it does not involve any parameters, hence the stored mask in the forward pass is used as a reference for the backpropagation update path, giving ΔC_r^3 .

Step2: (Inverse of step 4 in the forward path)

Calculating $\Delta k_{q,r}^3$:

$$\begin{aligned} \Delta k_{q,r}^3(u, v) &= \frac{\partial L}{\partial k_{q,r}^3(u, v)} = \sum_i^{13} \sum_j^{13} \frac{\partial L}{\partial C_r^3(i, j)} \frac{\partial C_r^3(i, j)}{\partial k_{q,r}^3(u, v)} \\ &= \sum_i^{13} \sum_j^{13} \Delta C_r^3(i, j) \cdot \frac{\partial C_r^3(i, j)}{\partial t} \frac{\partial t}{\partial k_{q,r}^3(u, v)}; \quad t = (\sum_q M_q^1 * k_{q,r}^3 + b_r^3) \end{aligned}$$

$$\begin{aligned}
 &= \sum_i^{13} \sum_j^{13} \Delta C_r^3(i, j) \cdot f' \cdot \frac{\partial(\sum_q M_q^1 * k_{q,r}^3 + b_r^3)}{\partial k_{q,r}^3(u, v)} \\
 &= \sum_i^{13} \sum_j^{13} \Delta C_r^3(i, j) \cdot f' \cdot M_q^1(i - u, j - v) \\
 \text{Let } &\Delta C_{r,f}^3(i, j) = \Delta C_r^3(i, j) \cdot f'
 \end{aligned}$$

Hence, we get a deconvolution as follows:

$$\Delta k_{q,r}^3(u, v) = \sum_i^{13} \sum_j^{13} M_q^1(i - u, j - v) \cdot \Delta C_{r,f}^3(i, j)$$

Here, $M_q^{1^{inv}}$ which is equivalent to convolving with the inverse of M_q^1 i.e. rotating M_q^1 by 180° (flipped)

$$\Delta k_{q,r}^3 = M_q^{1^{inv}} * \Delta C_{r,f}^3$$

Calculating ΔM_q^1 :

Similarly, following the above process for ΔM_q^1 , we get similar deconvolution:

$$\begin{aligned}
 C_r^3 &= f(\sum_q M_q^1 * k_{q,r}^3 + b_r^3); \\
 \Delta M_q^1(i, j) &= \frac{\partial L}{\partial M_q^1(i, j)} \\
 \Delta M_q^1 &= \sum_r^{15} \Delta C_{r,f}^3 * k_{q,r}^{3^{inv}}
 \end{aligned}$$

Calculating Δb_r^3 :

$$\begin{aligned}
 \Delta b_r^3 &= \frac{\partial L}{\partial b_r^3} = \sum_i^{13} \sum_j^{13} \frac{\partial L}{\partial C_r^3(i, j)} \frac{\partial C_r^3(i, j)}{\partial b_r^3} \\
 &= \sum_i^{13} \sum_j^{13} \Delta C_r^3(i, j) \cdot \frac{\partial C_r^3(i, j)}{\partial t} \frac{\partial t}{\partial b_r^3}; \quad t = (\sum_q M_q^1 * k_{q,r}^3 + b_r^3) \\
 &= \sum_i^{13} \sum_j^{13} \Delta C_r^3(i, j) \cdot f' \cdot \frac{\partial(\sum_q M_q^1 * k_{q,r}^3 + b_r^3)}{\partial b_r^3} \\
 &= \sum_i^{13} \sum_j^{13} \Delta C_{r,f}^3(i, j) \cdot f' \\
 \Delta b_r^3 &= \sum_i^{13} \sum_j^{13} \Delta C_{r,f}^3(i, j)
 \end{aligned}$$

Step3: (Inverse of step 3 in the forward path)

Since it is a max-pool operation, it does not involve any parameters, the stored mask in the forward pass is used as a reference for backpropagation. Updates from ΔM_q^1 will be propagated into respective ΔC_q^2 .

Step4: (Inverse of step 2 in the forward path)

Calculating $\Delta k_{p,q}^2$:

$$\begin{aligned}
 \Delta k_{p,q}^2(u, v) &= \frac{\partial L}{\partial k_{p,q}^2(u, v)} = \sum_i^{46} \sum_j^{46} \frac{\partial L}{\partial C_q^2(i, j)} \frac{\partial C_q^2(i, j)}{\partial k_{p,q}^2(u, v)} \\
 &= \sum_i^{46} \sum_j^{46} \Delta C_q^2(i, j) \cdot \frac{\partial C_q^2(i, j)}{\partial t} \frac{\partial t}{\partial k_{p,q}^2(u, v)}; \quad t = (\sum_p C_p^1 * k_{p,q}^2 + b_q^2) \\
 &= \sum_i^{46} \sum_j^{46} \Delta C_q^2(i, j) \cdot f' \cdot \frac{\partial (\sum_p C_p^1 * k_{p,q}^2 + b_q^2)}{\partial k_{p,q}^2(u, v)}
 \end{aligned}$$

Equivalently,

$$\Delta k_{p,q}^2 = C_p^{1^{inv}} * \Delta C_{q,f}^2$$

Calculating ΔC_p^1 :

Similarly, following the above process for ΔM_q^1 , we get similar deconvolution:

$$\Delta C_p^1(i, j) = \frac{\partial L}{\partial C_p^1(i, j)}$$

$$\Delta C_q^1 = \sum_q^{48} \Delta C_{q,f}^2 * k_{p,q}^{2^{inv}}$$

Calculating Δb_q^2 :

$$\Delta b_q^2 = \frac{\partial L}{\partial b_q^2} = \sum_i^{46} \sum_j^{46} \frac{\partial L}{\partial C_q^2(i, j)} \frac{\partial C_q^2(i, j)}{\partial b_q^2}$$

$$\Delta b_q^2 = \sum_i^{46} \sum_j^{46} \Delta C_{q,f}^2(i, j)$$

Step5: (Inverse Of step 1 in the forward path)

Calculating $\Delta k_{1,p}^1$:

$$\Delta k_{1,p}^1(u, v) = \frac{\partial L}{\partial k_{1,p}^1(u, v)} = \sum_i^{50} \sum_j^{50} \frac{\partial L}{\partial C_p^1(i, j)} \frac{\partial C_p^1(i, j)}{\partial k_{1,p}^1(u, v)}$$

Equivalently,

$$\Delta k_{1,p}^1 = I^{inv} * \Delta C_{p,f}^1$$

Calculating Δb_p^1 :

$$\Delta b_p^1 = \frac{\partial L}{\partial b_p^1} = \sum_i^{50} \sum_j^{50} \frac{\partial L}{\partial C_p^1(i, j)} \frac{\partial C_p^1(i, j)}{\partial b_p^1}$$

$$\Delta b_p^1 = \sum_i^{50} \sum_j^{50} \Delta C_{p,f}^1(i, j)$$

5.2 Gaussian Noise

The probability density function $p(x)$ for a Gaussian distribution is:

$$p(x) = \frac{1}{\sqrt{2\pi\sigma^2}} e^{\frac{-(x-\mu)^2}{2\sigma^2}}$$

where μ is the mean

σ is the standard deviation

σ^2 is the variance

The generated noise is then added onto the image as

$$\tilde{z} = z + n$$

where z is the noise-free image

n is the noise with Gaussian distribution with desired variance (noise)

5.3 Traditional denoising methods

Gaussian filtering:

In this, the source image is convolved with the selected Gaussian filter for denoising.

The Gaussian distribution in 1-D has the form:

$$G(x) = \frac{1}{\sqrt{2\pi\sigma^2}} e^{\frac{-x^2}{2\sigma^2}}$$

where σ is the standard deviation of the distribution. (Here, it is assumed that the distribution has a mean of zero)

Library used – OpenCV (cv2)

Parameters used – kernel size – 3*3 (standard)

Link to the library - https://docs.opencv.org/master/d4/d86/group__imgproc__filter.html#gaabe8c836e97159a9193fb0b11ac52cf1

Average filtering:

Average (or mean) filtering is a method of ‘smoothing’ images by reducing the amount of intensity variation between neighbouring pixels. The average filter works by moving through the image pixel by pixel, replacing each value with the average value of neighbouring pixels, including itself.

The function smooths an image using the kernel:

$$K = \frac{1}{kernel_{height} * kernel_{width}} \begin{bmatrix} 1 & \dots & 1 \\ \vdots & \ddots & \vdots \\ 1 & \dots & 1 \end{bmatrix}$$

Library used – OpenCV (cv2)

Parameters used – kernel size – 3*3

Link to the library - https://docs.opencv.org/master/d4/d86/group__imgproc__filter.html#ga8c45db9afe636703801b0b2e440fce37

Median filtering:

Median filtering is a non-linear method used to remove noise from images. It is widely used as it is very effective at removing noise while preserving edges. It is particularly effective at removing ‘salt and pepper’ type noise. The image is smoothed using the median filter with the kernel size \times kernel size aperture. Each channel of a multi-channel image is processed independently.

Library used – OpenCV (cv2)

Parameters used – kernel size – 3*3

Link to the library - https://docs.opencv.org/master/d4/d86/group__imgproc__filter.html#ga564869aa33e58769b4469101aac458f9

Bilateral filtering:

The basic idea underlying bilateral filtering is to do in the range of an image that traditional filters do in its domain. Two pixels can be close to one another, that is, occupy the nearby spatial location, or they can be similar to one another, that is, have nearby values, possibly in a perceptually meaningful fashion. Bilateral Filter can reduce unwanted noise very well while keeping edges fairly sharp.

Library used – OpenCV (cv2)

Parameters used – $kernelSize = 3$, $sigmaColor = 3$, $sigmaSpace = 3$

Link to the library - https://docs.opencv.org/master/d4/d86/group__imgproc__filter.html#ga9d7064d478c95d60003cf839430737ed

bm3d filtering:

bm3d is based on an enhanced sparse representation in the transform-domain. The enhancement of the sparsity is achieved by grouping similar 2D image fragments (e.g. blocks) into 3D data arrays which we call "groups".

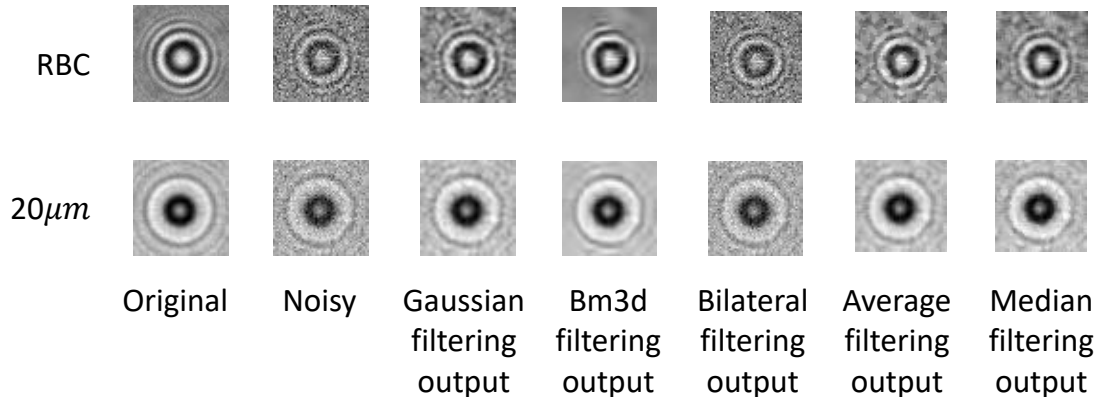
Image fragments are grouped based on similarity, but unlike standard k-means clustering and such cluster analysis methods, the image fragments are not necessarily disjoint. This block-matching algorithm is less computationally demanding.

Library used – bm3d

Parameters used – $\sigma_{psd} = 15$

Link to library - <https://pypi.org/project/bm3d/>; <http://www.cs.tut.fi/~foi/GCF-BM3D/>

5.4 Comparison of the denoised outputs from various modalities



5.5 SNR of individual samples of various cell types

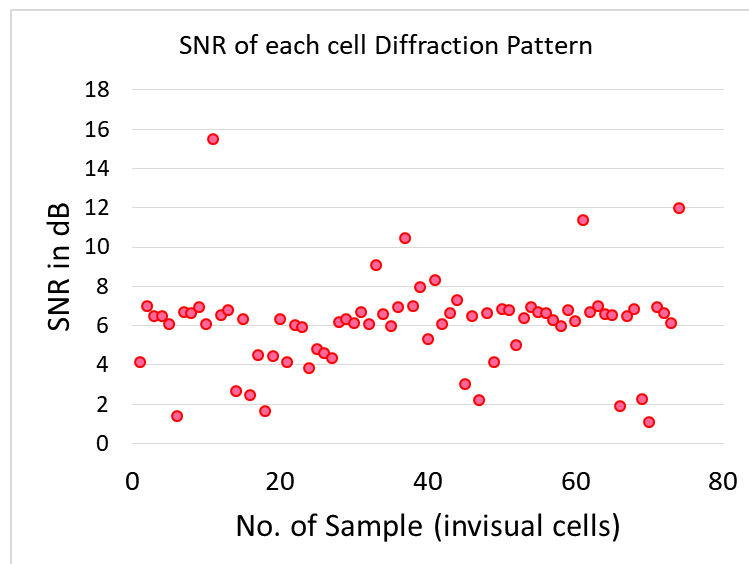
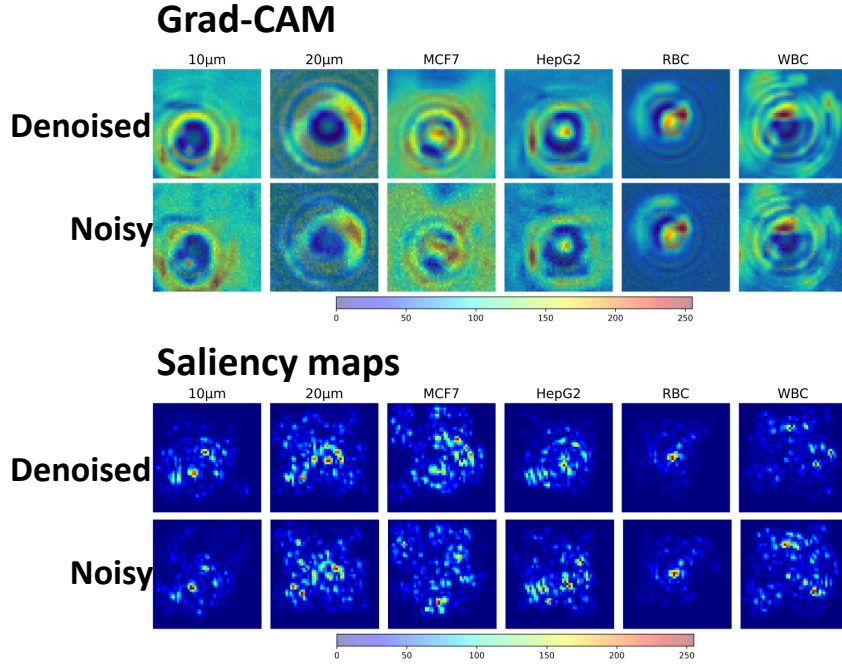


Figure 8: Graph depicting the variation in SNR of individual samples of various cell types denoised by the CNN Autoencoder

5.6 Grad-CAM and Saliency maps of the individual cell-lines



Grad-CAM is a technique to measure the cumulative activations from all the layers of the network recorded across the image. It helps to localize the key regions in the image that contribute to the classification decision and provides a visual understanding of the same through the overlaid heat maps. As referenced from the colormap, the regions in red are of higher importance compared to those in blue. From a comparison of noisy and denoised samples, it is observed that the significant activations in the Grad-CAMs are recorded at the center and on the diffraction rings of the cell-lines. The noise in the images skews the activations by either diminishing them in regions of interest or by increasing activations outside those regions. This skew is however corrected by the denoising as shown in Fig. 5.6.

Again, Saliency Maps help to identify the differentiating regions of interest that have a significant role in determination of the class label of the images. From a comparison of saliency, it is observed that denoising suppresses the pseudo-important regions of interest that have been generated due to the noise in the image.